14th MEETING OF THE SCIENTIFIC COMMITTEE

7 to 12 September 2026, Tórshavn, Faroe Islands

SC14 - Eco 04
2025-2026 SPRFMO Southeastern Pacific Ecosystem Status Report

Ecosystems Working Group

2025-2026 SPRFMO SOUTHEASTERN PACIFIC ECOSYSTEM STATUS REPORT

A report of the Ecosystem Working Group to the Scientific Committee of the South Pacific Fisheries Management Organisation

Executive Summary

The 2025–2026 Ecosystem Status Report (ESR) provides a preliminary integrated assessment of environmental conditions across the eastern and southeastern Pacific, based on five regional domains spanning the Equatorial High Seas, Northern Humboldt, Northern Chile, Central-Southern Chile, and the Oceanic Southeast Pacific. The reporting period covers September 2025 to August 2026, with longer historical records used to place recent conditions in context.

The most prominent feature of the reporting period was the rapid development of El Niño conditions during the first half of 2026. Following predominantly negative ENSO conditions through 2024–2025 and into early 2026, tropical Pacific indicators shifted rapidly toward a warm state. This transition was accompanied by the eastward and upward propagation of warm subsurface waters across the equatorial Pacific and, by August 2026, strong warming of the upper eastern equatorial Pacific.

The regional expression of this transition was strongest in the Equatorial High Seas and Northern Humboldt. By August 2026, sea surface temperature anomalies reached +3.83°C and +3.17°C, respectively, compared with +1.77°C in Northern Chile, +0.81°C in Central-Southern Chile, and +0.75°C in the Oceanic Southeast Pacific. Sea level showed an even stronger meridional contrast, with detrended anomalies reaching +21.11 cm in the Equatorial High Seas and +8.03 cm in Northern Humboldt, while conditions farther south were substantially weaker or close to climatological levels. These patterns indicate that the developing tropical signal had already propagated strongly into the northern part of the ESR domain by the end of the reporting period.

Marine heatwaves were widespread during 2025–2026 but differed substantially among regions in their timing, duration, and intensity. Northern Chile experienced MHW conditions already during late 2025, preceding the more widespread development observed during 2026. Prolonged events subsequently occurred in the Equatorial High Seas, Northern Humboldt, and Northern Chile, while Central-Southern Chile and the Oceanic Southeast

Pacific were characterised primarily by more frequent but shorter events. Higher-intensity conditions were particularly evident in Northern Humboldt.

Responses of other ecosystem indicators were less spatially coherent than those of temperature and sea level. Coastal upwelling anomalies were predominantly negative during the reporting period and were negative in all three coastal regions by August 2026, with the strongest weakening in Northern Humboldt. Chlorophyll-a, however, showed no comparable basin-wide response: concentrations at the end of the reporting period were slightly below climatology in Northern Humboldt and Northern Chile, slightly above climatology in the Equatorial High Seas and Central-Southern Chile, and close to climatological conditions in the Oceanic Southeast Pacific. Upper-ocean structure and oxygen conditions also retained pronounced regional differences associated with the contrasting physical and biogeochemical regimes across the study area.

Taken together, the indicators show that the 2025–2026 ecosystem state was characterised by a rapidly developing large-scale warm event superimposed on strong regional heterogeneity. Temperature and sea level provided the clearest and most spatially coherent expression of the developing El Niño, whereas coastal upwelling, chlorophyll-a, marine heatwaves, and subsurface conditions exhibited more region-specific responses. This highlights the importance of evaluating ecosystem conditions through multiple complementary indicators rather than assuming a uniform response to basin-scale climate forcing.

Importantly, August 2026 represents the developmental phase rather than the culmination of the current El Niño event. The NOAA CPC outlook issued in August 2026 indicates a very high probability of El Niño persisting through the remainder of 2026 and early 2027, with strong-to-very-strong conditions favoured during late 2026. Consequently, environmental and ecosystem responses may continue to develop beyond the present ESR reporting period. Continued monitoring will be particularly important for assessing subsequent changes in upper-ocean temperature and sea level, coastal upwelling, oxygen conditions, marine heatwaves, and primary productivity.

SPRFMO
South Pacific Regional Fisheries Management Organisation

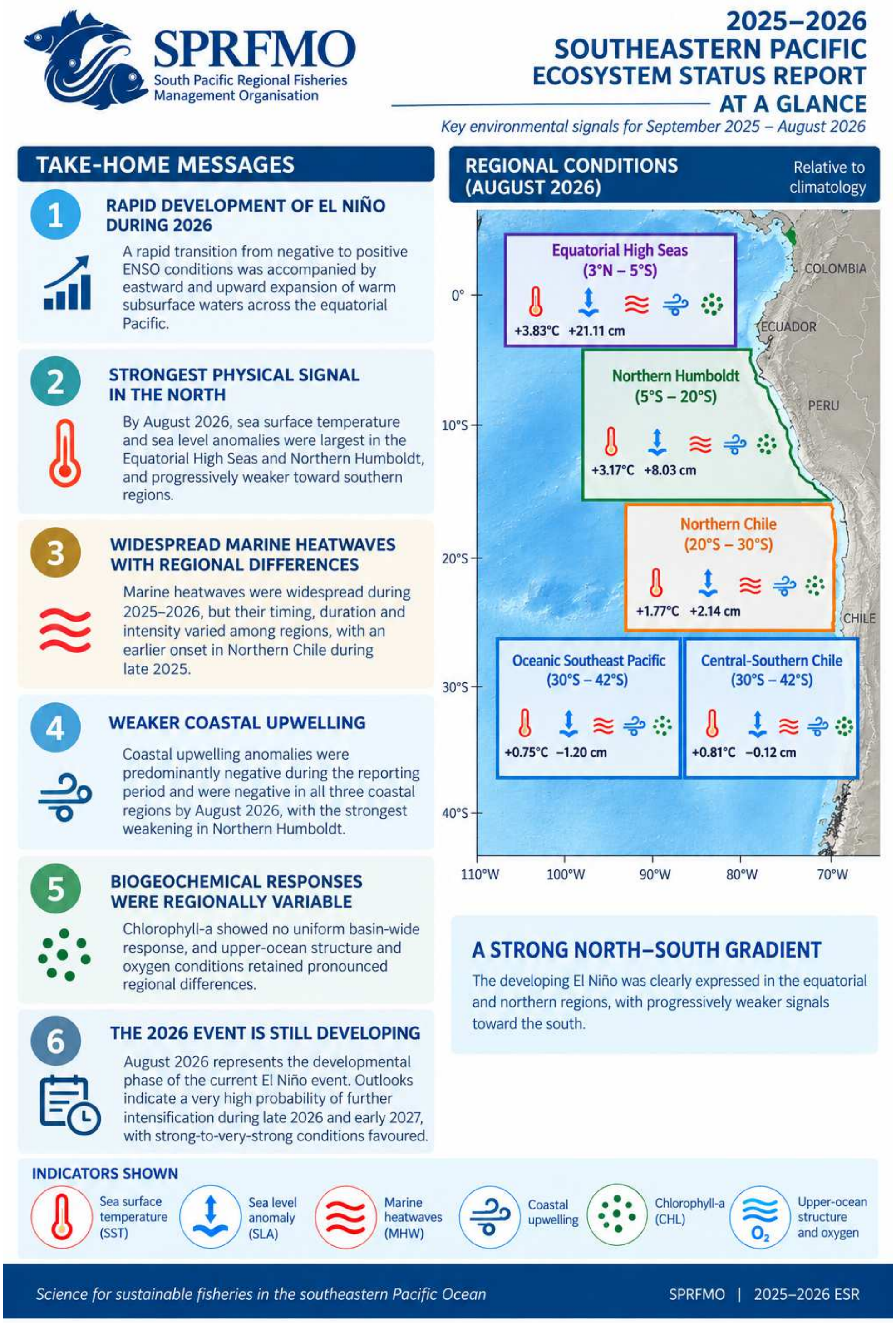

2025–2026 Ecosystem Status Report at a glance. The infographic and graphical elements were generated with the assistance of OpenAI ChatGPT, based on the environmental indicators, results, and interpretations presented in this report. All numerical values, scientific content, and final interpretations were reviewed by the authors.

Table of contents

Contributors

This report was prepared by the SPRFMO Ecosystem Working Group (EWG) with contributions from:

Rubén Luna Aguayo, Instituto de Investigación Pesquera, Chile
Cristian Salas Domínguez, Instituto de Investigación Pesquera, Chile
Sebastián Vásquez Pastene, Instituto de Investigación Pesquera, Chile

Suggested citation:

SPRFMO Ecosystem Working Group (2026). *2025–2026 SPRFMO Southeastern Pacific Ecosystem Status Report*. South Pacific Regional Fisheries Management Organisation.

1. Study area

The preliminary Ecosystem Status Report (ESR) was structured around five regional domains encompassing contrasting coastal and oceanic environments of the eastern and southeastern Pacific (Figure 1). The regions were defined to provide spatial units for the calculation and comparison of environmental and ecosystem indicators, while representing major latitudinal and coastal–oceanic contrasts across the study area.

The five regions were defined as follows: (1) Equatorial High Seas, extending from 3°N to 5°S and from 110°W to 90°W; (2) Northern Humboldt, extending from 5°S to 20°S and from 90°W to the South American coast; (3) Northern Chile, extending from 20°S to 30°S and from 85°W to the coast; (4) Central-Southern Chile, extending from 30°S to 42°S and from 85°W to the coast; and (5) Oceanic Southeast Pacific, extending from 30°S to 42°S and from 105°W to 85°W.

The regionalisation was designed to distinguish broad environmental domains rather than political or management jurisdictions. In particular, it separates the equatorial oceanic environment from the Northern Humboldt system and distinguishes the northern and central-southern sectors of the Chilean margin. An additional oceanic domain off central-southern Chile was included to allow coastal–oceanic contrasts in ecosystem conditions to be evaluated using a common set of indicators.

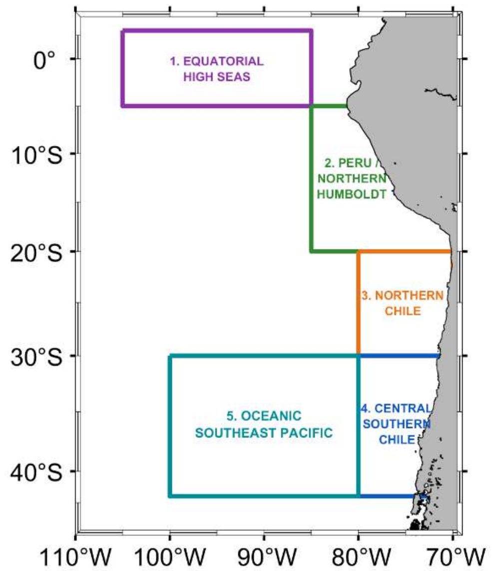

Figure 1. Regional domains used for the preliminary Ecosystem Status Report (ESR): (1) Equatorial High Seas (3°N–5°S, 110–90°W); (2) Northern Humboldt (5–20°S, 90°W–coast); (3) Northern Chile (20–30°S, 85°W–coast); (4) Central-Southern Chile (30–42°S, 85°W–coast); and (5) Oceanic Southeast Pacific (30–42°S, 105–85°W).

2. Sea surface temperature and thermal conditions

2.1. Data source

Sea surface temperature (SST) conditions were characterised using the Global Ocean Operational Sea Surface Temperature and Sea Ice Analysis (OSTIA) products distributed by the Copernicus Marine Service. OSTIA provides daily, gap-free Level-4 estimates of foundation SST on a 0.05° × 0.05° global grid, integrating satellite observations from infrared and microwave radiometers with in situ observations.

2.2. Methods: Regional time series and thermal anomalies

Thermal conditions were evaluated separately for the five regions defined for the preliminary Ecosystem Status Report (ESR): Equatorial High Seas, Northern Humboldt, Northern Chile, Central-Southern Chile, and Oceanic Southeast Pacific. For each region, gridded SST values were spatially averaged and aggregated into monthly means to generate regional SST time series.

Monthly SST anomalies (SSTA) were calculated relative to the long-term climatological mean for the corresponding calendar month:

$$SSTA_{y,m} = SST_{y,m} - S\bar{S}T_m ,$$

where $SST_{y,m}$is the regional mean SST for year $y$and month m, and $S\bar{S}T_m$is the climatological SST for the corresponding calendar month. Positive values represent warmer-than-average conditions, whereas negative values represent cooler-than-average conditions.

To characterise the persistence and temporal accumulation of thermal anomalies, cumulative SST anomalies were calculated as:

$$CSSTA_t = \sum_{i=1}^{t} S\,STA_i.$$

The cumulative anomaly was used as an integrated measure of the persistence of anomalously warm or cool conditions rather than as a formal statistical estimate of temperature trend. Periods characterised by a sustained increase in CSSTA indicate the predominance of positive SST anomalies, whereas sustained decreases indicate the predominance of negative anomalies. Changes in the slope of the cumulative curve therefore provide a means of identifying transitions between relatively warm and cool periods.

2.3. Results: regional SST and thermal anomalies

Sea surface temperature showed a pronounced seasonal cycle across all five ESR regions, superimposed on substantial interannual variability (Figure 2). Mean temperatures decreased progressively from the Equatorial High Seas and Northern Humboldt regions towards Northern and Central-Southern Chile, while the Oceanic Southeast Pacific showed intermediate conditions. The amplitude of the seasonal cycle was comparatively small in the Equatorial High Seas and increased towards the temperate regions.

Monthly SST anomalies revealed several coherent warm and cool periods across the study area, although their magnitude differed among regions. A particularly pronounced warm anomaly occurred during 1997–1998, with the strongest signal in the Equatorial High Seas and Northern Humboldt regions and a progressively weaker expression towards the south. Other periods of positive anomalies were evident around 2015–2016 and again during the most recent years. Conversely, persistent negative anomalies occurred during several periods, including the late 2000s and early 2020s, with particularly clear signals in the Chilean and oceanic regions.

The cumulative SST anomaly further highlighted differences in the persistence of thermal conditions among regions. The Equatorial High Seas and Northern Humboldt showed the largest cumulative fluctuations, including a sharp increase during the late 1990s followed by a prolonged decline through much of the 2000s and early 2010s. Northern Chile exhibited a broadly similar but weaker pattern, whereas cumulative anomalies in Central-Southern Chile and the Oceanic Southeast Pacific varied over a narrower range. All five regions showed an upward trajectory towards the end of the record, indicating the recent predominance of positive monthly SST anomalies.

By August 2026, positive SST anomalies were observed across all five ESR regions, with a marked latitudinal gradient in their magnitude. Monthly SST anomalies reached +3.83°C in the Equatorial High Seas, +3.17°C in Northern Humboldt, +1.77°C in Northern Chile, +0.81°C in Central-Southern Chile, and +0.75°C in the Oceanic Southeast Pacific (Figure 2). The recent warming signal was therefore strongest in the equatorial and northern regions and progressively weakened towards the southern and oceanic sectors.

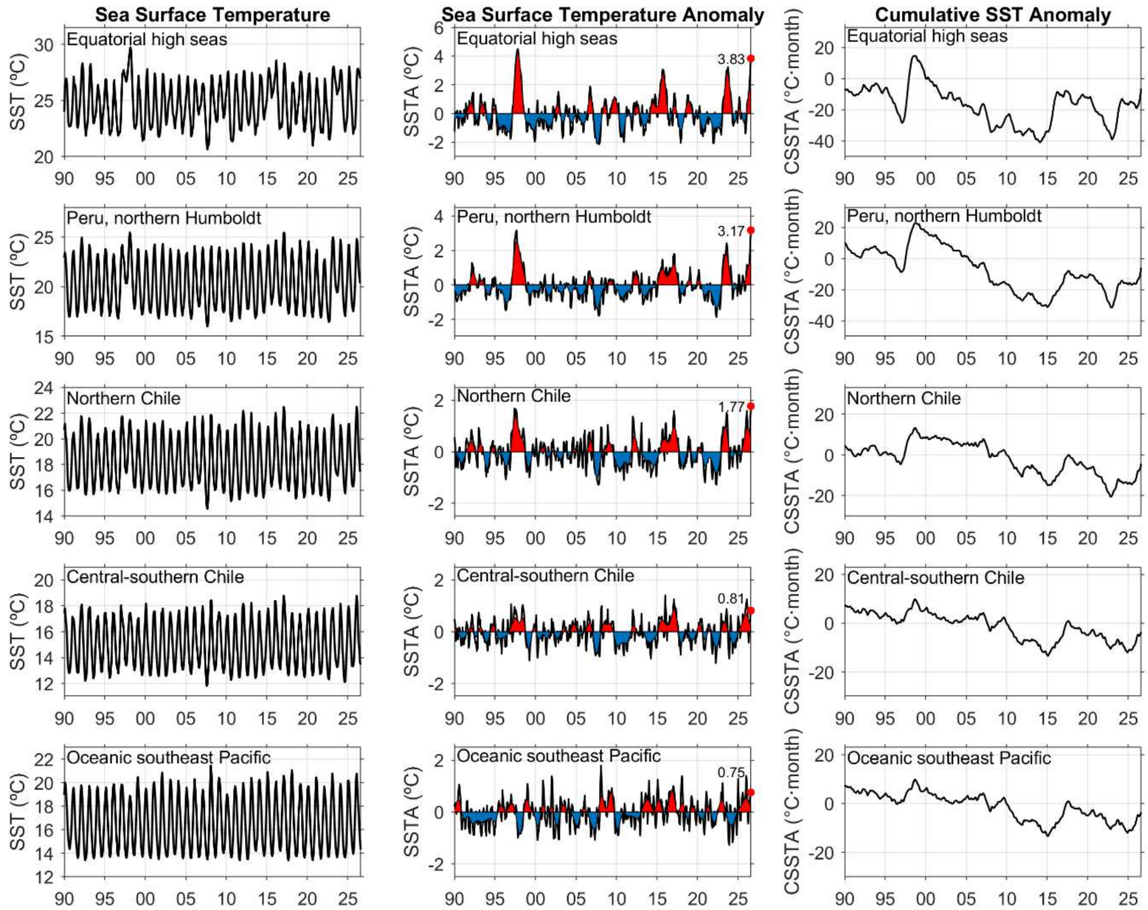

Figure 2. Monthly sea surface temperature (SST), SST anomalies (SSTA), and cumulative SST anomalies (CSSTA) for the five regions considered in the preliminary Ecosystem Status Report (ESR), from 1990 to August 2026. Left panels: regional mean monthly SST. Middle panels: monthly SST anomalies relative to the climatological monthly mean; positive and negative anomalies are shown in red and blue, respectively, and red dots indicate the most recent values (August 2026). Right panels: cumulative SST anomalies, calculated as the sequential sum of monthly SSTA, providing an integrated representation of the persistence of anomalously warm or cool conditions.

2.4. Methods: Spatial SST anomaly analysis

In addition to the regional time series, spatial SST anomalies were calculated at each grid cell to characterise the geographical extent and intensity of recent thermal conditions. Monthly SST anomaly fields were obtained by subtracting the long-term climatological SST for each calendar month from the corresponding monthly SST field:

$$SSTA_{x,y,m} = SST_{x,y,m} - S\bar{S}T_{x,m} ,$$

where x denotes an individual OSTIA grid cell.

Monthly anomaly maps were produced for September 2025–August 2026, providing a spatial representation of the most recent annual cycle considered in the preliminary ESR. These fields complement the regional indices by identifying spatial heterogeneity within and among ESR regions and by showing whether regional mean anomalies reflect spatially widespread conditions or more localised thermal features.

2.5. Results: spatial patterns of SST anomalies

Spatial SST anomalies showed substantial temporal and geographical variability during September 2025–August 2026 (Figure 3). During September–November 2025, thermal conditions were spatially heterogeneous, with generally weak anomalies across much of the study area and alternating areas of positive and negative anomalies. Positive anomalies became more widespread from December 2025 onwards, particularly in the southeastern Pacific between approximately 20°S and 40°S.

During January–March 2026, positive SST anomalies persisted over extensive areas of the eastern South Pacific, including the Northern Humboldt and Northern Chile regions and adjacent oceanic waters. In contrast, cooler-than-average conditions developed farther south, particularly south of approximately 35–40°S during March and April, producing a pronounced meridional contrast in SST anomalies.

From May 2026 onwards, the spatial distribution changed markedly, with increasingly strong and widespread positive anomalies developing in the equatorial and northern sectors. This warming intensified through June and July and was most pronounced by August 2026, when anomalies exceeding +3°C occupied extensive areas of the equatorial eastern Pacific and Northern Humboldt region, with locally stronger anomalies approaching or exceeding +5°C. Positive anomalies also extended southward along the South American margin and into the subtropical Southeast Pacific, although their magnitude generally decreased towards the south.

The spatial fields therefore indicate that the positive regional SST anomalies observed in August 2026 (Figure 2) were part of the broad-scale warming pattern shown in Figure 3, rather than isolated local features. However, the magnitude and temporal development of the warming were spatially heterogeneous, with the strongest anomalies concentrated in the equatorial and northern portions of the ESR study area.

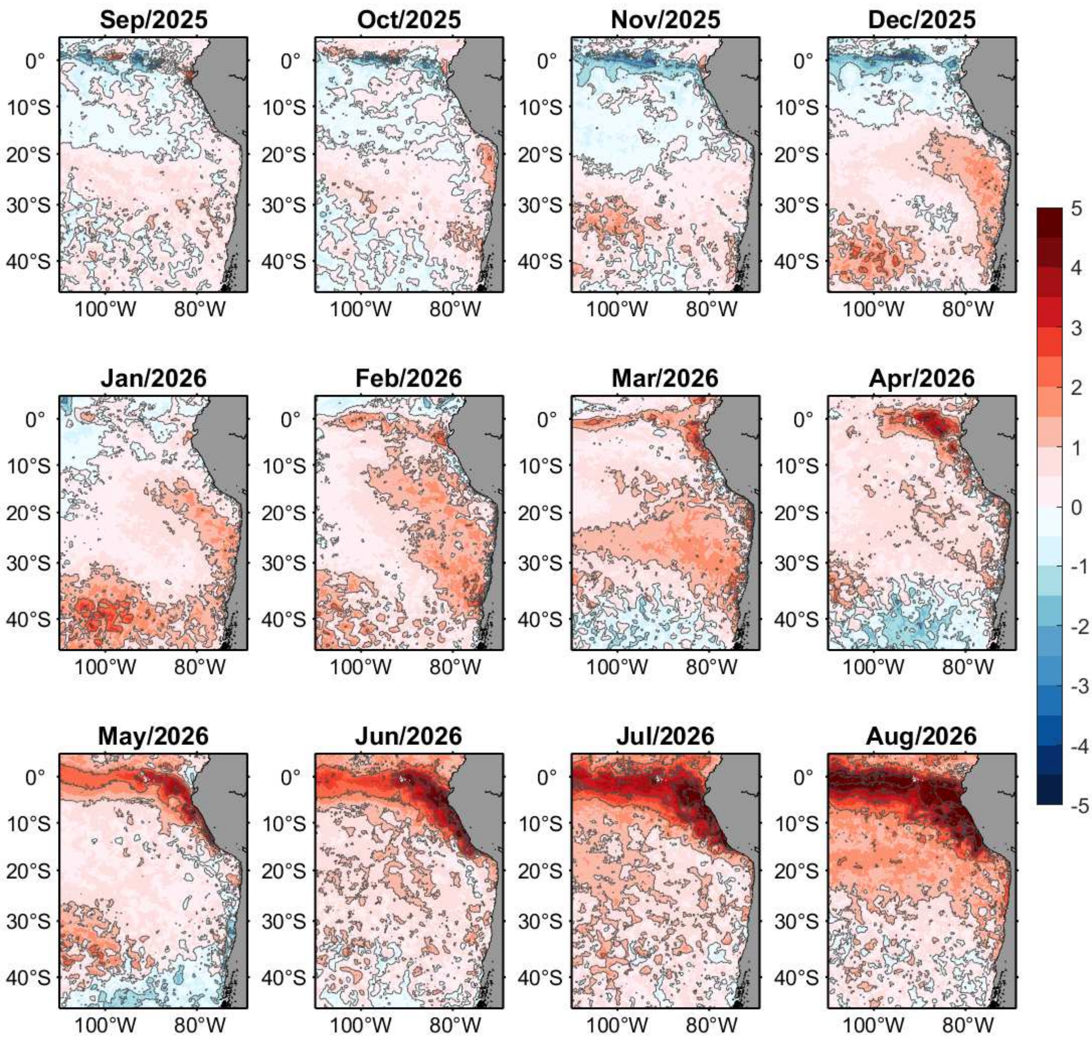

Figure 3. Spatial distribution of monthly sea surface temperature anomalies (SSTA) across the ESR study area from September 2025 to August 2026. Anomalies were calculated at each OSTIA grid cell relative to the corresponding climatological monthly mean. Positive (red) and negative (blue) values indicate warmer- and cooler-than-average conditions, respectively. Contours indicate the spatial distribution and magnitude of SST anomalies. Units are °C.

3. Marine heatwaves and cold spells

3.1. Methods: Marine heatwave and cold-spell identification

Marine heatwaves (MHWs) and marine cold spells (MCSs) were identified from the daily regional SST time series derived from OSTIA (Section 2), following the framework proposed by Hobday et al. (2016, 2018). For each ESR region, daily climatological mean SST and the corresponding 90th and 10th percentile thresholds were calculated for each calendar day and smoothed using a 15-day locally weighted regression.

MHWs were defined as periods during which daily SST exceeded the seasonally varying 90th percentile threshold for at least five consecutive days (Hobday et al., 2016). Conversely, MCSs were identified using the corresponding lower-tail criterion, with SST below the 10th percentile threshold for at least five consecutive days. Events separated by gaps of up to two days were treated as a single event. The analysis was conducted continuously across 2025 and 2026, allowing events extending across the end of a calendar year to be identified as a single event.

For each event, duration and thermal intensity relative to the climatological threshold were calculated. MHW intensity was classified according to the four-category framework of Hobday et al. (2018), based on multiples of the difference between the climatological mean and the 90th percentile threshold: Category I (Moderate), Category II (Strong), Category III (Severe), and Category IV (Extreme). An equivalent classification was applied to cold conditions relative to the 10th percentile threshold. Regional summaries included the number of events, cumulative event days, maximum event duration, and number of days assigned to each intensity category.

3.2. Results: Marine heatwaves and cold spells

Marine heatwaves were detected across all five ESR regions during 2025–2026, but their frequency, duration, timing, and intensity differed substantially among regions (Figure 4). In contrast, marine cold spells were largely absent during the period analysed, with only a single short cold event detected in the Equatorial High Seas.

The Equatorial High Seas showed the longest individual event, with one MHW lasting 113 days during 2026. All 113 MHW days were classified as Category I. This was also the only region where a marine cold spell was detected, consisting of a single 7-day event during 2025.

In the Northern Humboldt region, three MHWs accounted for 106 days, including one prolonged event lasting 86 days during the second half of 2026. This region showed the greatest diversity in MHW intensity, with 65, 26, 10, and 6 days classified as Categories I, II, III, and IV, respectively. Two shorter events of 8 and 12 days were also detected during early 2026. No marine cold spells were identified.

The Northern Chile region experienced six MHWs totalling 179 days, including a particularly persistent event lasting 109 days during early 2026. Most MHW days were classified as Category I (142 days), with an additional 34 Category II days. Notably, MHW conditions were already detected in Northern Chile during late 2025, including events before the transition into 2026, whereas comparable MHW conditions in the other ESR regions generally emerged during 2026. This asynchronous onset highlights the regional character of the thermal conditions preceding the more widespread MHW development observed during 2026.

In Central-Southern Chile, MHW activity was more fragmented. Eleven events were identified, accounting for 190 days, the largest cumulative number of MHW days among the five regions, although the longest individual event lasted only 29 days. Most MHW conditions were moderate, with 177 days classified as Category I and 5 days as Category II. Events occurred during both 2025 and 2026, but were generally shorter and more recurrent than the prolonged events observed farther north.

The Oceanic Southeast Pacific also exhibited recurrent MHW activity, with nine events totalling 136 days and a maximum individual duration of 33 days. All classified MHW days were Category I, indicating predominantly moderate conditions. As in Central-Southern Chile, the thermal signal was characterised by multiple relatively short events rather than the prolonged episodes observed in the northern regions.

Overall, MHW conditions during 2025–2026 were widespread but strongly heterogeneous in their temporal expression across the ESR study area. The northern regions were characterised by fewer but substantially longer-lasting events, including the 113-day event in the Equatorial High Seas and the 109-day event in Northern Chile, whereas Central-Southern Chile and the Oceanic Southeast Pacific generally experienced a larger number of shorter events. Higher-intensity MHW conditions were particularly evident in the Northern Humboldt region, while conditions in the Equatorial High Seas and Oceanic Southeast Pacific remained predominantly moderate.

The timing of MHW onset also differed among regions. In particular, Northern Chile experienced MHW conditions during late 2025 before the development of the more widespread events observed across the ESR regions during 2026. Together with the marked differences in event duration and intensity among regions, this temporal asynchrony indicates that the expression of MHW conditions was not spatially uniform and suggests that regional-scale processes may modulate the manifestation of broader thermal anomalies across the study area.

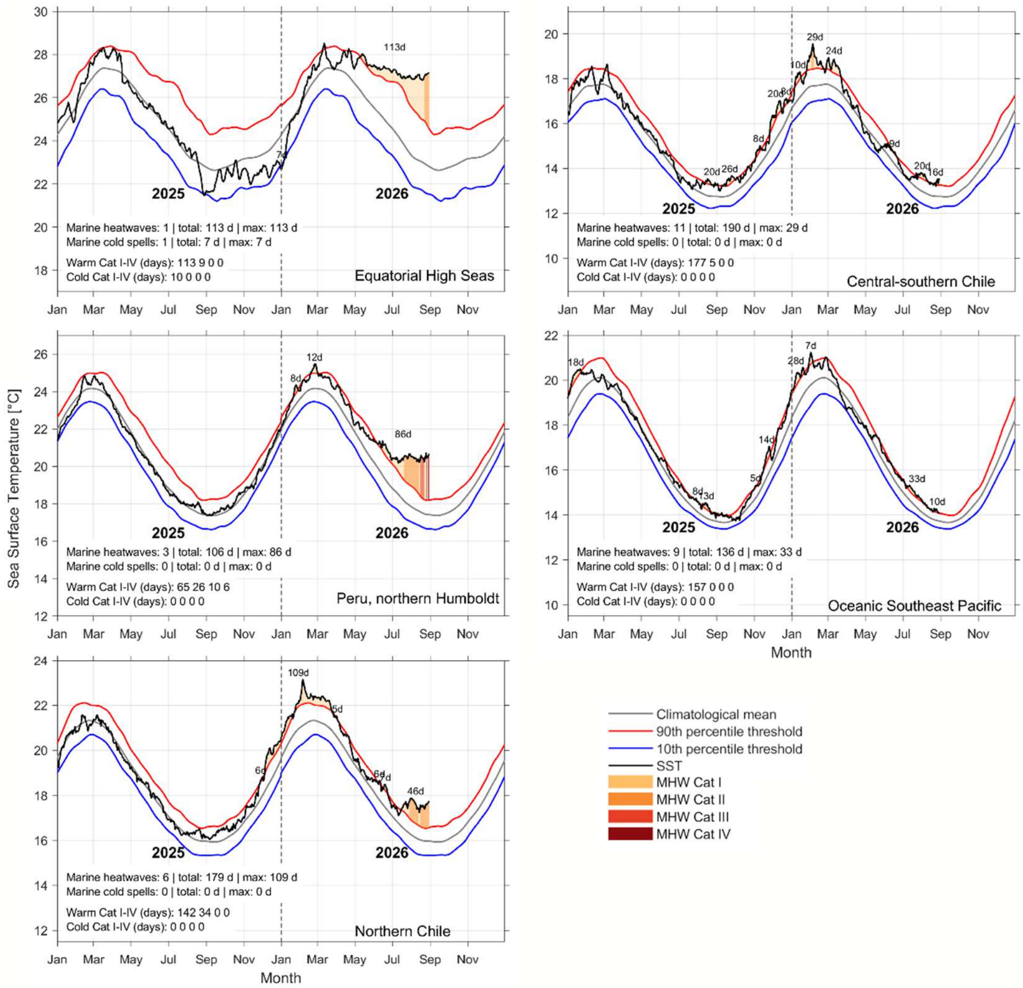

Figure 4. Marine heatwaves (MHWs) and marine cold spells (MCSs) across the five regions considered in the preliminary Ecosystem Status Report (ESR) during 2025–2026. Black lines show daily sea surface temperature (SST), grey lines the daily climatological mean, and red and blue lines the seasonally varying 90th and 10th percentile thresholds, respectively. Shaded areas indicate MHW intensity according to Categories I–IV (Moderate, Strong, Severe, and Extreme), while numbers indicate the duration (days) of individual events. The vertical dashed line marks the transition between 2025 and 2026. Insets summarise the number of MHW and MCS events, cumulative event days, maximum event duration, and the number of days within each intensity category.

4. Sea level conditions

4.1. Data source

Sea level conditions were characterised using daily sea level anomaly (SLA) fields from the Global Ocean Gridded L4 Sea Surface Heights and Derived Variables product distributed by the Copernicus Marine Service. SLA represents variations in sea surface height relative to a reference mean sea surface and was analysed over the five regions defined for the preliminary Ecosystem Status Report (ESR).

Daily SLA fields were spatially averaged within each ESR region and subsequently aggregated into monthly means. SLA values were converted from metres to centimetres for analysis and presentation. The historical record available from the product was used to characterise long-term variability, while September 2025–August 2026 was considered the reporting period for the current ESR.

4.2. Methods: Regional sea level variability and long-term change

Regional monthly SLA time series were calculated by spatially averaging all valid grid cells within each ESR region, accounting for the decrease in grid-cell area with latitude through cosine-latitude weighting. Because SLA contains both long-term sea-level change and shorter-term variability, these components were analysed separately. A linear trend was fitted independently to the monthly SLA series of each region. The fitted trend was retained as an estimate of long-term sea-level change and expressed in mm yr^{-1}.

To characterise interannual sea-level variability independently of this long-term change, the fitted linear trend was subtracted from each regional SLA time series. The mean detrended SLA for each calendar month was subsequently calculated over the historical record and removed from the corresponding monthly values. The resulting detrended SLA anomalies therefore represent departures from the typical seasonal conditions after removal of the linear long-term change.

A 12-month running mean of the original monthly SLA series was additionally calculated to illustrate low-frequency sea-level variability while retaining the long-term signal. This running mean was used for visualisation rather than as a formal estimate of trend.

4.3. Results: Regional sea level variability and long-term change

Sea level anomaly showed substantial temporal variability across all five ESR regions, superimposed on a persistent increase over the historical record (Figure 5). Linear trends were positive and relatively consistent among regions, ranging from 2.48 to 2.96 mm yr^{-1}. Estimated rates were 2.57 mm yr^{-1} in the Equatorial High Seas, 2.48 mm yr^{-1} in Northern Humboldt, 2.63 mm yr^{-1} in Northern Chile, 2.74 mm yr^{-1} in Central-Southern Chile, and 2.96 mm yr^{-1} in the Oceanic Southeast Pacific. The 12-month running means similarly showed progressively higher SLA during the latter part of the record, although substantial interannual and decadal variability was superimposed on this long-term increase.

After removal of the linear trend and climatological seasonal cycle, marked differences in interannual sea-level variability were evident among regions. The largest departures occurred in the Equatorial High Seas, including a pronounced positive event during 1997–1998 and additional positive anomalies around 2015–2016 and during the most recent period. These signals were also apparent in Northern Humboldt but with lower amplitude, while variability was generally weaker farther south.

During the September 2025–August 2026 reporting period, a pronounced positive sea-level anomaly progressively developed in the equatorial and northern sectors. By August 2026, detrended SLA reached +21.11 cm in the Equatorial High Seas and +8.03 cm in Northern Humboldt, while a substantially weaker positive anomaly (+2.14 cm) occurred in Northern Chile. Conditions were close to the climatological expectation in Central-Southern Chile and slightly negative in the Oceanic Southeast Pacific. The end of the reporting period was therefore characterised by a strong meridional gradient in detrended sea-level conditions, with exceptionally elevated values concentrated in the equatorial and northern portions of the study area.

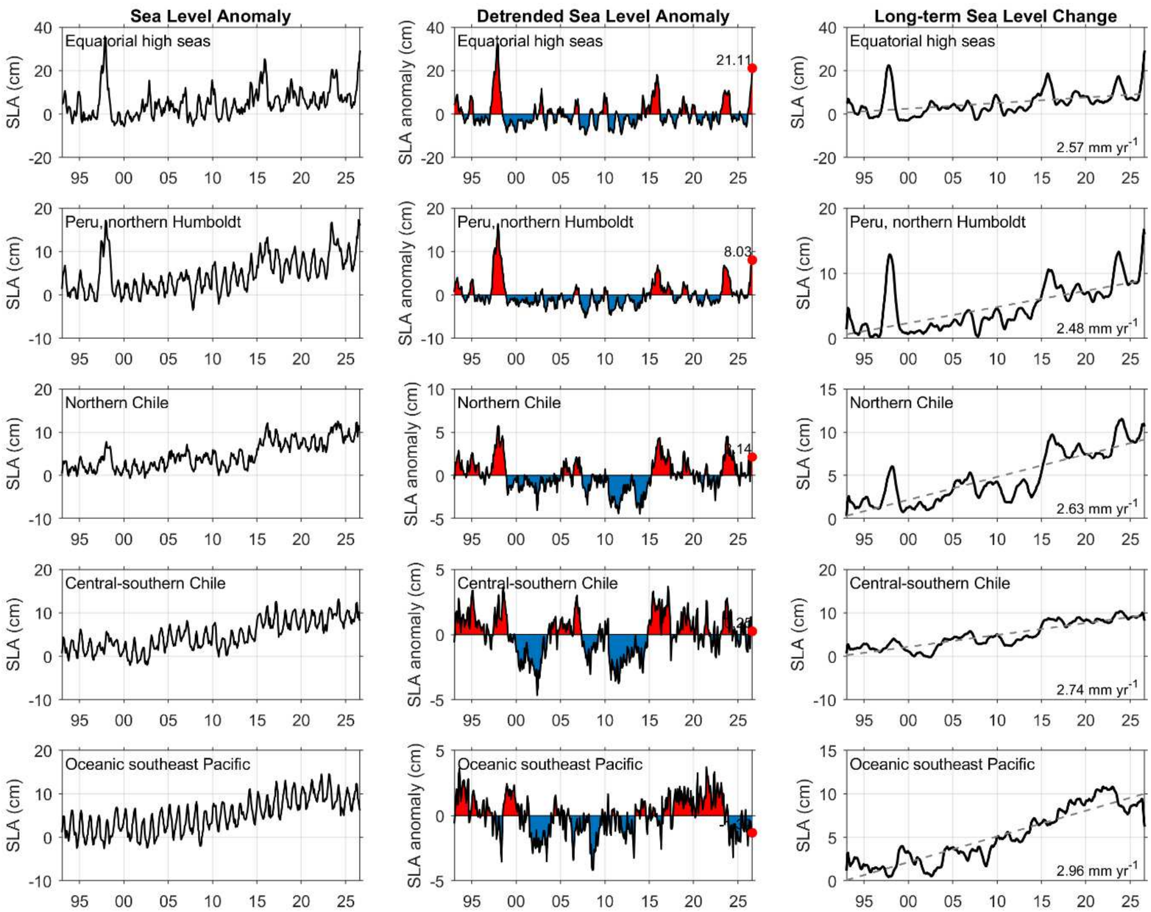

Figure 5. Regional sea level variability across the five Ecosystem Status Report (ESR) regions. Left: monthly sea level anomaly (SLA). Centre: detrended SLA anomalies, calculated after removal of the regional linear trend and climatological seasonal cycle; positive and negative anomalies are shown in red and blue, respectively, with August 2026 highlighted. Right: 12-month running mean of SLA (black line) and fitted linear long-term trend (grey dashed line), with estimated rates of sea-level change indicated for each region. SLA is expressed in centimetres and trends in mm yr^{-1}.

4.4. Methods: Spatial sea level anomaly analysis

To examine the spatial structure of recent sea-level conditions, monthly SLA fields were calculated from the daily gridded observations for September 2025–August 2026. Monthly fields were expressed in centimetres and mapped using a common scale across all months, allowing changes in both the magnitude and geographical distribution of SLA to be compared throughout the reporting period.

These spatial fields complement the regional time series by identifying within-region heterogeneity and by determining whether changes in regional mean SLA represent spatially extensive conditions or more localised features. Unlike the regional detrended anomalies described above, the spatial maps show the original SLA fields, thereby retaining both long-term sea-level change and shorter-term variability.

4.5. Results: Spatial sea level conditions

Spatial SLA patterns showed substantial geographical and temporal variability during September 2025–August 2026 (Figure 6). During September–November 2025, SLA was comparatively low across the equatorial eastern Pacific, while higher and spatially heterogeneous values occurred farther south. Positive SLA became more widespread during December 2025 and early 2026, although substantial spatial heterogeneity remained across the study area.

A distinct large-scale positive sea-level signal developed in the equatorial and northern eastern Pacific during the first half of 2026. The feature became increasingly evident from March–April and intensified substantially from May 2026 onwards, expanding across the Equatorial High Seas and towards the Northern Humboldt region. By June–August, the highest SLA values were concentrated across the equatorial eastern Pacific and adjacent northern sector.

By August 2026, this development resulted in a pronounced meridional contrast, with strongly elevated SLA across the equatorial and northern eastern Pacific and considerably lower values toward Northern Chile, Central-Southern Chile, and the Oceanic Southeast Pacific. This spatial pattern was consistent with the regional detrended time series, which showed that the strong positive sea-level conditions at the end of the reporting period were concentrated primarily in the Equatorial High Seas and Northern Humboldt regions.

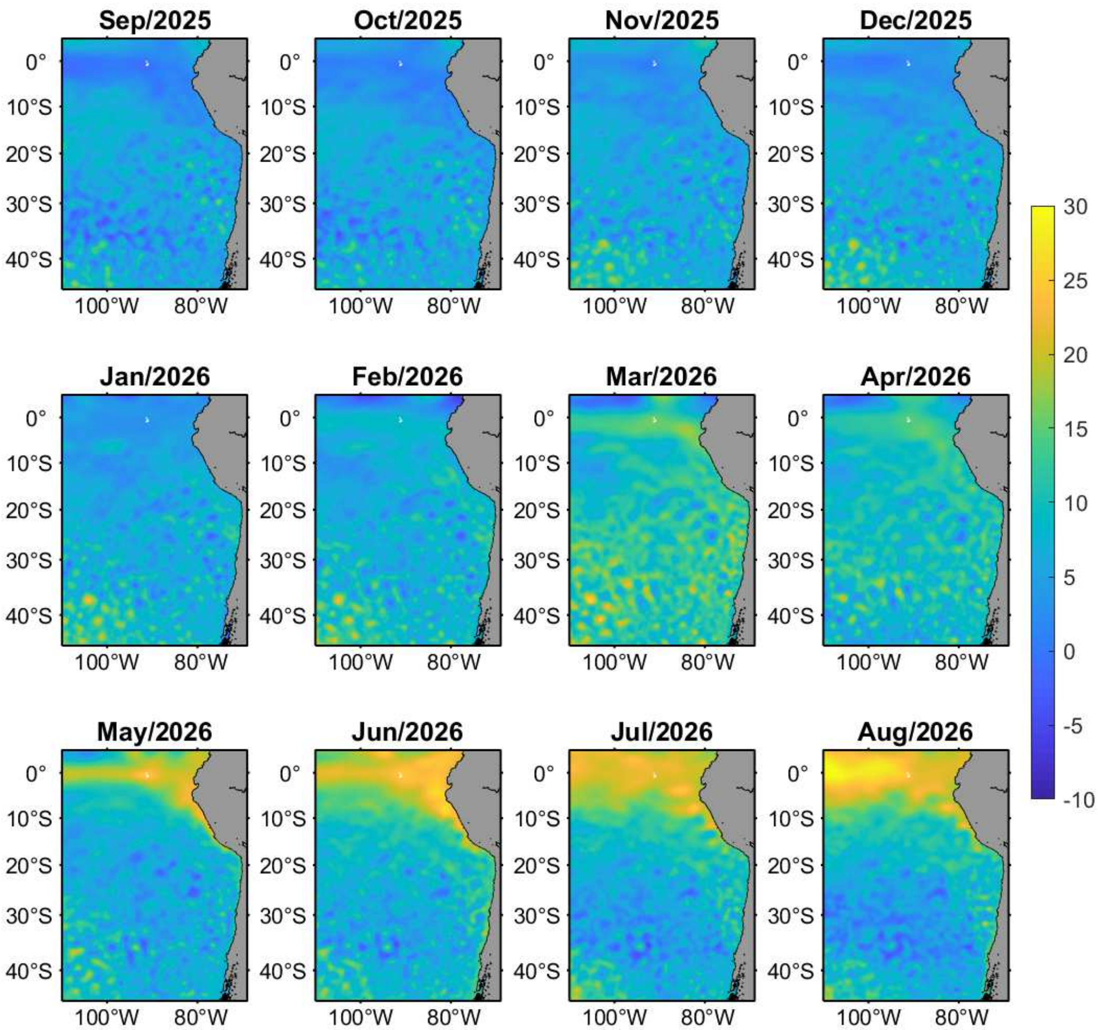

Figure 6. Monthly sea level anomaly (SLA) fields across the Southeast Pacific during the ESR reporting period, from September 2025 to August 2026. SLA is expressed in centimetres, with a common colour scale applied to all months to facilitate comparison of the magnitude and spatial distribution of sea-level conditions through time. These maps show the original SLA fields and therefore retain both long-term sea-level change and shorter-term variability.

5. Coastal upwelling conditions

5.1. Data source

Coastal upwelling conditions were characterised using daily 10-m wind fields from the ERA5 atmospheric reanalysis. Zonal (*u*) and meridional (*v*) wind components were used to estimate wind stress and the associated surface Ekman transport along the eastern boundary of the Southeast Pacific.

The analysis focused on three coastal ESR regions: Northern Humboldt (Peru), Northern Chile, and Central-Southern Chile. For each region, representative coastal bands extending up to 200 km offshore were used to characterise regional-scale wind-driven upwelling conditions.

5.2. Methods: Coastal upwelling index

Daily wind stress components were calculated from the ERA5 10-m wind fields as:

$$\tau_x = \rho_a C_D \mid U \mid u$$
$$\tau_y = \rho_a C_D \mid U \mid v$$

where ρ_a is air density (1.225 kg m^{-3}), C_D is a constant drag coefficient (1.3×10^{-3}), and $\mid U \mid$ is wind speed.

Ekman transport was subsequently calculated as:

$$M_x = \frac{\tau_y}{\rho_w f}$$
$$M_y = -\frac{\tau_x}{\rho_w f}$$

where ρ_w is seawater density (1025 kg m^{-3}) and f is the latitude-dependent Coriolis parameter.

To account for changes in coastline orientation, Ekman transport was projected onto a local offshore unit vector derived from the smoothed orientation of the continental coastline. The resulting cross-shore Ekman transport was used as the Coastal Upwelling Index (UI), with positive values representing offshore Ekman transport and therefore upwelling-favourable conditions, and negative values representing onshore transport.

Regional daily indices were calculated as area-weighted means within representative 200-km coastal bands. The bands covered 12–18°S for Northern Humboldt, 20–30°S for Northern Chile, and 32–38°S for Central-Southern Chile. Grid-cell values were weighted by the cosine of latitude to account for differences in cell area.

Daily indices were aggregated into monthly means. For each region, a monthly climatology was calculated over the available historical record, and monthly UI anomalies were obtained by subtracting the corresponding climatological monthly mean from each observation:

$$UI'_{y,m} = UI_{y,m} - \bar{U}I_m$$

where $UI_{y,m}$ is the monthly upwelling index for year y and month m, and $\bar{UI}_m$ is the long-term climatological mean for that calendar month.

Cumulative UI anomalies were subsequently calculated as the cumulative sum of the monthly anomalies. Increasing cumulative anomalies therefore indicate sustained periods of stronger-than-average upwelling-favourable transport, whereas decreasing values indicate persistent weaker-than-average conditions. The current ESR reporting period extends from September 2025 to August 2026.

5.3. Results: Regional coastal upwelling variability

Coastal upwelling conditions showed pronounced seasonal and interannual variability across the three regions, with predominantly positive monthly UI values indicating that offshore, upwelling-favourable Ekman transport was the prevailing condition over most of the historical record (Figure 7). The magnitude and variability of the index were greatest in Northern Humboldt, while Northern Chile showed lower variability and Central-Southern Chile displayed the largest occurrence of monthly values approaching or falling below zero.

The monthly anomaly series revealed substantial differences in low-frequency variability among regions. In Northern Humboldt, predominantly negative anomalies characterised the early part of the record, followed by an extended period of generally stronger-than-average upwelling conditions from approximately the late 1990s through the early 2010s. Thereafter, anomalies became progressively more negative, with weaker-than-average conditions prevailing during much of the most recent decade. This transition is particularly evident in the cumulative anomaly series, which increased markedly from the late 1990s to the early-to-mid 2010s before declining persistently towards 2026.

Northern Chile exhibited a broadly similar but substantially weaker low-frequency pattern. The cumulative anomaly decreased during the early 1990s, subsequently increased through the 2000s and first half of the 2010s, and then declined during the most recent decade. By the end of the reporting period, the cumulative anomaly had returned close to its initial level, indicating that the prolonged positive anomalies of the intermediate period had largely been offset by more recent weaker-than-average upwelling conditions.

Central-Southern Chile showed a different temporal pattern. The cumulative anomaly declined through much of the 1990s and 2000s, reaching its lowest values around the late 2000s, before recovering during the following decade. A particularly marked increase occurred from approximately 2017 to the early 2020s, indicating a sustained period of stronger-than-average upwelling-favourable transport. More recently, this positive tendency weakened, and the cumulative index declined during the latter part of the record.

During the September 2025–August 2026 ESR reporting period, monthly anomalies were predominantly negative across the three coastal regions, although individual months showed considerable variability. By August 2026, the UI anomaly was negative in all three regions, with the largest negative departure occurring in Northern Humboldt, followed by Central-Southern Chile and Northern Chile. Together with the downward trajectories of the cumulative anomaly curves toward the end of the record, these results indicate weaker-than-average wind-driven upwelling conditions during the most recent period, particularly in Northern Humboldt.

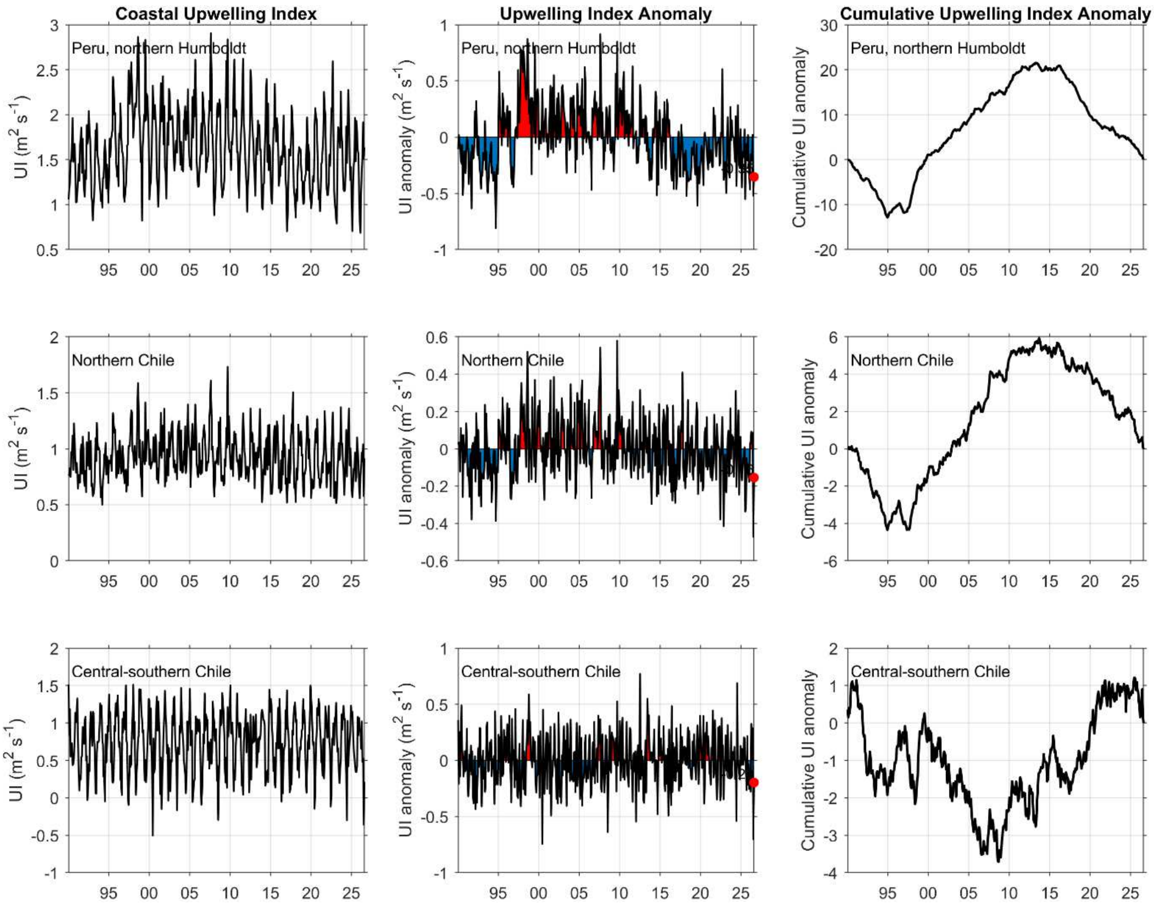

Figure 7. Regional variability in the Coastal Upwelling Index (UI) across the three coastal Ecosystem Status Report (ESR) regions. Left: monthly area-weighted cross-shore Ekman transport, with positive values indicating offshore, upwelling-favourable transport. Centre: monthly UI anomalies relative to the long-term monthly climatology; positive and negative anomalies are shown in red and blue, respectively, with August 2026 highlighted. Right: cumulative monthly UI anomalies, where increasing and decreasing trajectories indicate sustained periods of stronger- and weaker-than-average upwelling-favourable transport, respectively. UI is expressed in $m^2 s^{-1}$.

6. Mixed layer depth, subsurface oxygen, and oxycline dynamics

6.1. Data source

Mixed layer depth (MLD) and dissolved oxygen at 100 m were obtained from the Global Ocean Physics Reanalysis (GLOBAL_MULTIYEAR_PHY_001_030) and the Global Ocean Biogeochemistry Hindcast (GLOBAL_MULTIYEAR_BGC_001_029) products distributed by the Copernicus Marine Service, without splicing to the near-real-time analysis and forecast systems. Both products span the period from January 1993 onward, with the physical reanalysis extending through June 2026 and the biogeochemical hindcast through May 2026. MLD was obtained at 0.083° horizontal resolution and 50 vertical levels; dissolved oxygen was obtained at 0.25° horizontal resolution and 75 vertical levels using the PISCES biogeochemical model.

6.2. Methods: Regional time series

The same five regions used elsewhere in this report were used here: Equatorial High Seas, Northern Humboldt, Northern Chile, Central-Southern Chile, and Oceanic Southeast Pacific. For each region and each month, MLD and 100 m oxygen values were averaged spatially, weighted by grid-cell area, to produce a single regional value. Oxycline depth was computed profile by profile within each region and then summarised as the regional median.

6.3. Results: regional patterns in MLD, oxygen, and the oxycline

Mixed layer depth follows a clear seasonal rhythm almost everywhere, but the strength of that rhythm changes a lot from north to south. In the Equatorial High Seas the mixed layer stays shallow year-round, rarely exceeding 20–30 m, with only a few of sharper spikes standing out, related with El Niño events (1997-1998, 2015-2016). Moving south, seasonal deepening becomes progressively more pronounced: Northern Humboldt cycles between roughly 10 and 60 m, Northern Chile between 15 and nearly 80 m, and also show a few maximus related with El Niño (1997-1998, 2007, 2010, 2019 y 2024), and Central-Southern Chile shows a similar range. The Oceanic Southeast Pacific is the most extreme case among the five, with winter mixing regularly pushing past 80 m and, in recent years, occasionally beyond 100 m, well past what the other regions ever reach (Figure 8).

Dissolved oxygen at 100 m tells a different regional story, one shaped less by seasons than by the strength of the oxygen minimum zone. The Equatorial High Seas and Northern Humboldt sit within that low-oxygen core, with concentrations mostly between 85 and 150 mmol m^{-3}; both show a sharp spike around 1997–1998, followed in Northern Humboldt by a long decline through the 2000-2015 that points to an expanding, more intense minimum zone, then partial recovery after roughly 2015 and a further dip around 2020–2022. Northern Chile and Central-Southern Chile sit outside the core of the minimum zone and hold higher, steadier values, Northern Chile zone gently declining toward a trough near 2010 before recovering. The Oceanic Southeast Pacific stays consistently the most oxygenated region in the record, with values above 250 mmol m^{-3} throughout (Figure 8).

Oxycline depth broadly mirrors the oxygen patterns, but adds a vertical dimension to the story. In the Equatorial High Seas and Northern Humboldt, where the minimum zone is strongest, the oxycline sits shallow, mostly within 40–70 m, keeping low-oxygen water close to the surface; Northern Humboldt shows a marked temporary deepening during the 1997–

1998 event, when the oxycline dropped toward 100–110 m before returning to its usual depth. Northern Chile shows a deeper and irregular oxycline, generally between 50 and 100 m with a brief shallowing during the same 1997–1998 period. Central-Southern Chile and the Oceanic Southeast Pacific show the deepest and most variable oxyclines of all five regions, frequently exceeding 150 m and at times reaching close to 300 m, consistent with the weaker, more diffuse oxygen minimum found in these more oceanic waters (Figure 8).

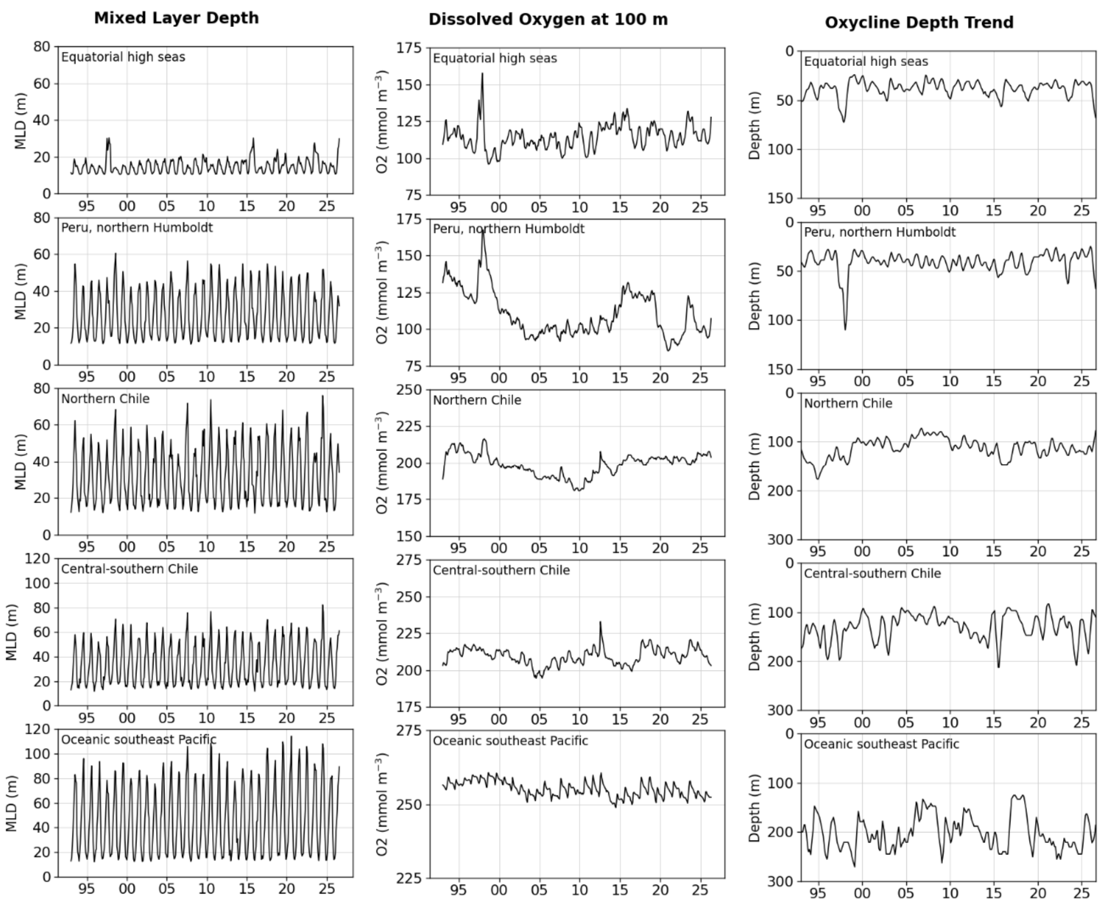

Figure 8. Long-term variability in upper-ocean vertical structure and oxygen conditions across the five Ecosystem Status Report (ESR) regions. Left: monthly regional mixed layer depth (MLD). Centre: monthly dissolved oxygen concentration at 100 m depth. Right: regional median oxycline depth derived from individual vertical oxygen profiles; the depth axis is reversed so that shallower oxycline conditions appear toward the top. Regional values were calculated from the Copernicus Marine physical reanalysis and biogeochemical hindcast products over their respective periods of availability (1993–2026). MLD and oxycline depth are expressed in metres, and dissolved oxygen in mmol m^{-3}.

7. Chlorophyll-a conditions

7.1. Data source

Surface chlorophyll-a concentration (CHL) was obtained from the Global Ocean Colour (Copernicus-GlobColour), Bio-Geo-Chemical, Level 3 daily satellite product (OCEANCOLOUR_GLO_BGC_L3_MY_009_103) distributed by the Copernicus Marine Service. The product provides globally gridded satellite ocean-colour observations at approximately 4-km spatial resolution and daily temporal resolution from September 1997 onwards. It combines observations from multiple ocean-colour satellite missions, including SeaWiFS, MODIS, MERIS, VIIRS and Sentinel-3 OLCI.

Chlorophyll-a concentration, expressed in mg m^{-3}, was used as an indicator of surface phytoplankton biomass. The complete historical record available for the analysis was used to provide long-term context, while September 2025–August 2026 was considered the reporting period for the preliminary ESR.

7.2. Methods: Regional chlorophyll-a time series and anomalies

The same five ESR regions used for the physical indicators were considered: Equatorial High Seas, Northern Humboldt, Northern Chile, Central-Southern Chile, and Oceanic Southeast Pacific. Daily satellite CHL observations were aggregated into monthly fields, and regional monthly values were calculated by spatially averaging all valid ocean grid cells within each region, accounting for differences in grid-cell area with latitude.

For each region, a climatological monthly cycle was calculated from the historical record. Monthly chlorophyll-a anomalies (CHLA) were then estimated as the difference between each monthly regional value and the corresponding long-term climatological mean for that calendar month:

$$CHLA_{y,m} = CHL_{y,m} - C\bar{H}L_m$$

where $CHL_{y,m}$represents chlorophyll-a concentration in year $y$and month m, and $C\bar{H}L_m$is the long-term climatological mean for month m.

Cumulative chlorophyll-a anomalies were calculated as the cumulative sum of monthly anomalies. Increasing trajectories therefore represent sustained periods in which chlorophyll-a concentrations were predominantly above the seasonal climatology, whereas decreasing trajectories indicate persistent below-average conditions. These cumulative anomalies were used to characterise low-frequency changes in chlorophyll conditions rather than as formal estimates of temporal trend.

7.3. Results: Regional chlorophyll-a variability

Chlorophyll-a concentration showed pronounced regional differences in both magnitude and seasonal variability (Figure 7). The highest concentrations occurred in the coastal regions, particularly Northern Humboldt and Central-Southern Chile, where monthly concentrations frequently approached or exceeded 1 mg m^{-3}. Northern Chile showed intermediate concentrations, whereas substantially lower values characterised the Equatorial High Seas and especially the Oceanic Southeast Pacific, reflecting the comparatively oligotrophic conditions of the oceanic domain.

The regional anomaly series revealed substantial low-frequency variability superimposed on the seasonal cycle. In the Equatorial High Seas, anomalies were generally small, although several short-lived departures occurred throughout the record. Cumulative anomalies increased strongly during the early part of the satellite record, subsequently declined for more than a decade, and remained predominantly negative during much of the period after the mid-2010s. The latest monthly anomaly was slightly positive (+0.03 mg m^{-3}).

Northern Humboldt exhibited substantially greater variability. Strong negative anomalies occurred near the beginning of the satellite record, followed by predominantly positive conditions during the early 2000s. Alternating positive and negative periods subsequently occurred, with relatively frequent positive anomalies from approximately the mid-2010s through the early 2020s. The cumulative anomaly remained negative for most of the historical record but increased markedly during the most recent decade, approaching its initial level by 2026. The August 2026 anomaly was slightly negative (−0.08 mg m^{-3}).

In Northern Chile, chlorophyll-a increased from relatively low values at the beginning of the record and subsequently fluctuated around comparatively stable concentrations for much of the 2000s and 2010s. The cumulative anomaly declined strongly during the first years of the record, followed by a prolonged recovery that reached positive values during the early 2020s. More recently, this trajectory reversed, consistent with predominantly negative anomalies toward the end of the record. By August 2026, CHLA was −0.08 mg m^{-3}.

Central-Southern Chile displayed strong seasonal variability and a gradual increase in regional chlorophyll-a concentrations over much of the record. Its cumulative anomaly declined until approximately the mid-2010s and then increased markedly, consistent with a prolonged period dominated by positive anomalies. Although considerable month-to-month variability persisted during 2025–2026, the August 2026 anomaly remained slightly positive (+0.039 mg m^{-3}).

The Oceanic Southeast Pacific showed the lowest chlorophyll-a concentrations and smallest absolute anomalies among the five regions. Cumulative anomalies declined during the first decade of the record, subsequently recovered gradually, and remained close to neutral during the most recent years. Chlorophyll-a conditions in August 2026 were essentially climatological (−0.0005 mg m^{-3}).

Overall, the end of the September 2025–August 2026 reporting period was characterised by contrasting regional conditions: slightly above-average chlorophyll-a in the Equatorial High Seas and Central-Southern Chile, below-average concentrations in Northern Humboldt and Northern Chile, and near-climatological conditions in the Oceanic Southeast Pacific.

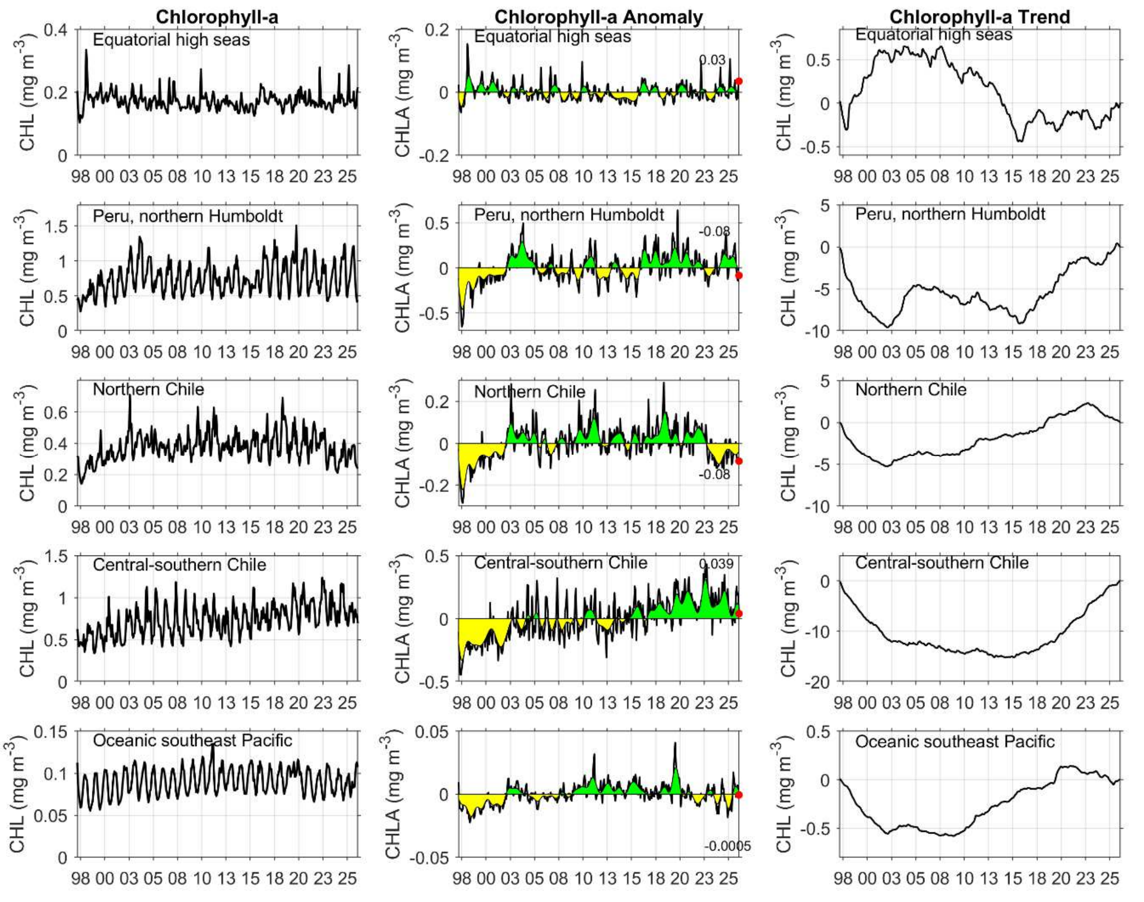

Figure 9. Regional chlorophyll-a variability across the five Ecosystem Status Report (ESR) regions. Left: monthly surface chlorophyll-a concentration. Centre: monthly chlorophyll-a anomalies relative to the long-term monthly climatology; positive and negative anomalies are shown in green and yellow, respectively, with August 2026 highlighted. Right: cumulative monthly chlorophyll-a anomalies, where increasing and decreasing trajectories

indicate sustained periods of above- and below-average chlorophyll-a conditions, respectively. Chlorophyll-a concentration and anomalies are expressed in mg m^{-3}.

7.4. Methods: Spatial chlorophyll-a analysis

Monthly chlorophyll-a fields were examined for September 2025–August 2026 to characterise the spatial distribution of surface phytoplankton biomass during the ESR reporting period. Monthly fields were derived from the satellite observations and displayed using a common logarithmic colour scale because chlorophyll-a concentrations span more than two orders of magnitude across the study domain.

The spatial analysis was used to complement the regional indices by resolving coastal–oceanic gradients and identifying geographically localised changes that may not be evident from regional averages.

7.5. Results: Spatial chlorophyll-a conditions

Monthly chlorophyll-a fields showed a persistent and pronounced coastal–oceanic gradient throughout the reporting period (Figure 10). Elevated concentrations were consistently associated with the eastern boundary and coastal waters of Peru and Chile, whereas low concentrations dominated the offshore subtropical Southeast Pacific.

From September 2025 through the austral summer of 2025–2026, relatively high chlorophyll-a concentrations persisted along much of the Peruvian coast and locally along Chile. In contrast, an extensive low-chlorophyll region occupied the offshore subtropical domain, particularly between approximately 20°S and 30°S. This oligotrophic feature remained evident throughout the annual cycle, although its geographical extent and intensity varied among months.

During the first half of 2026, coastal chlorophyll-a remained elevated along Peru, while concentrations in the offshore and Chilean sectors showed considerable spatial heterogeneity. Toward July–August 2026, enhanced chlorophyll-a became particularly evident in the equatorial eastern Pacific near the South American coast, whereas much of the subtropical oceanic region continued to exhibit low concentrations.

By August 2026, the spatial distribution therefore remained strongly heterogeneous, with locally elevated chlorophyll-a in the equatorial and coastal eastern Pacific contrasting with low concentrations across much of the offshore subtropical domain. This spatial structure highlights that the relatively small regional anomalies observed at the end of the reporting period can coexist with pronounced local gradients in surface phytoplankton biomass.

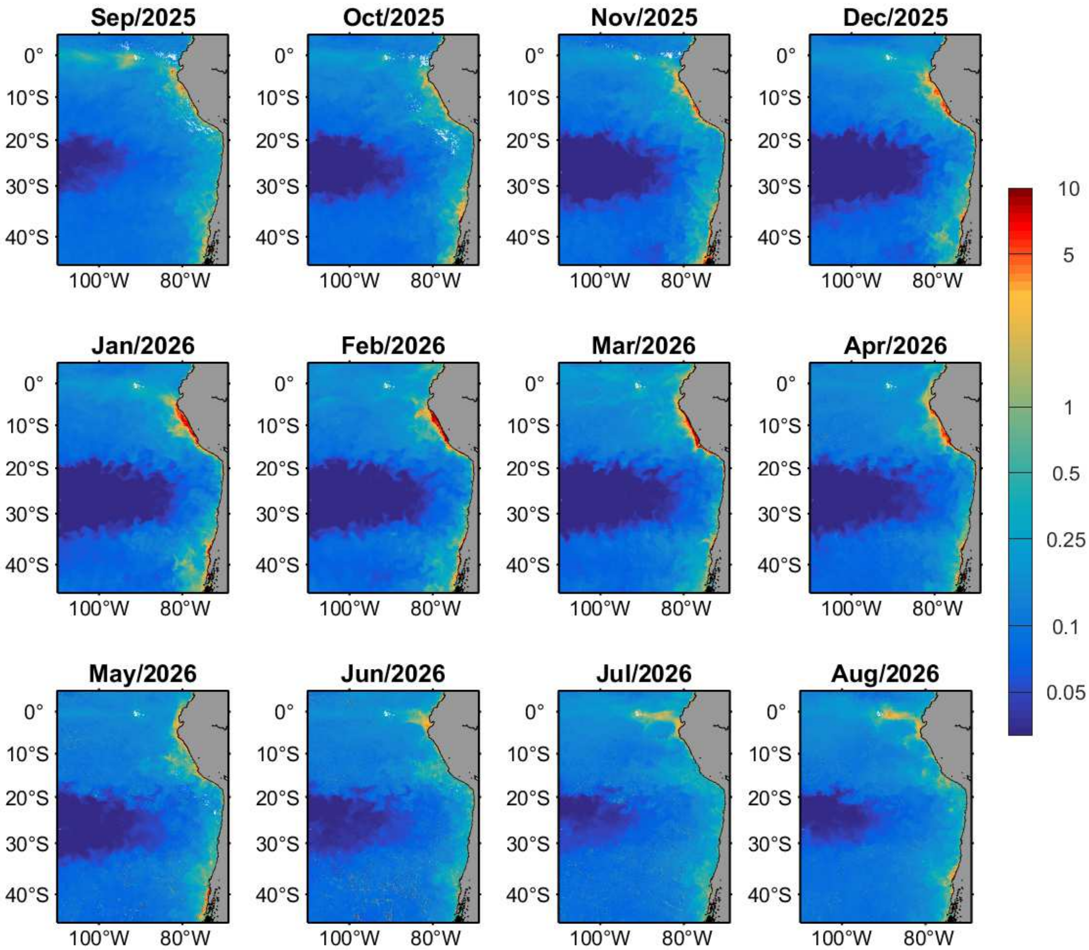

Figure 10. Monthly surface chlorophyll-a concentration across the Southeast Pacific during the ESR reporting period, from September 2025 to August 2026. Chlorophyll-a is expressed in mg m^{-3} and displayed using a common logarithmic colour scale across all months to facilitate comparison of coastal–oceanic gradients and changes in the spatial distribution of surface phytoplankton biomass through time.

8. El Niño–Southern Oscillation conditions and outlook

8.1. Data sources and ENSO indicators

The evolution of the El Niño–Southern Oscillation (ENSO) was characterised using complementary indicators from the NOAA Climate Prediction Center (CPC) and NOAA Physical Sciences Laboratory. These included the **Relative Oceanic Niño Index (RONI)**, the **Multivariate ENSO Index version 2 (MEI.v2)**, equatorial Pacific subsurface temperature anomalies, and the official CPC ENSO probability and event-strength outlooks issued in August 2026.

RONI characterises ENSO-related sea surface temperature variability in the Niño-3.4 region relative to the contemporaneous tropical mean state, while MEI.v2 integrates multiple oceanic and atmospheric variables to represent the coupled state of the tropical Pacific. Their joint evolution was examined from 1995 through August 2026 to place current conditions in a longer-term ENSO context.

The development of the 2026 event was further examined using monthly longitude–depth sections of equatorial Pacific temperature anomalies for September 2025–August 2026. These indicators were considered alongside the regional environmental conditions described elsewhere in this ESR, particularly SST, SLA, upper-ocean structure, coastal upwelling and chlorophyll-a.

Observed conditions through August 2026 were explicitly distinguished from the CPC forecast extending beyond the ESR reporting period. Consequently, projections concerning the subsequent magnitude and persistence of the event are presented as an outlook rather than as observed characteristics of the 2026 event.

8.2. Historical context and development of the 2026 El Niño

The historical evolution of MEI.v2 and RONI shows the alternating warm and cold phases of ENSO over the past three decades, including the major warm events of 1997–1998 and 2015–2016, as well as the prolonged cold conditions that characterised several recent years (Figure 11). Although the two indices differ in magnitude and temporal evolution, their major positive and negative phases are broadly consistent, providing complementary evidence of the large-scale coupled state of the tropical Pacific.

The period preceding the current event was dominated by negative ENSO indices. Both indicators remained predominantly negative through much of 2024–2025 and into early 2026. A rapid transition subsequently occurred during 2026. RONI changed sharply from negative to positive values, while MEI.v2 also moved from negative conditions toward a warm-phase state. By August 2026, RONI had increased to strongly positive values, indicating that the transition represented one of the most rapid warm-phase developments evident in the recent record.

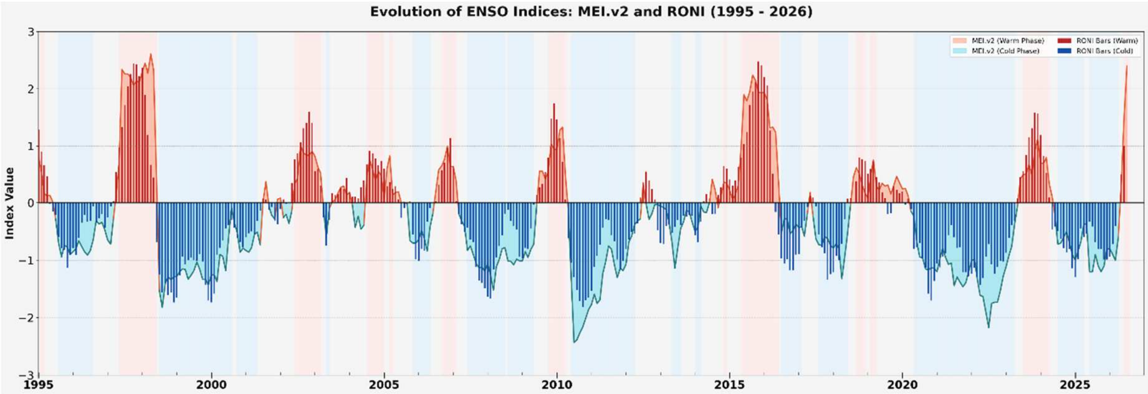

Figure 11. Evolution of the Multivariate ENSO Index version 2 (MEI.v2) and the Relative Oceanic Niño Index (RONI) from 1995 to August 2026. Warm and cold phases identified by MEI.v2 are indicated by red and blue background shading, respectively, while positive and negative RONI values are shown by red and blue bars. The historical series provides context for the rapid transition from negative ENSO conditions in 2025–early 2026 to strongly positive conditions by August 2026.

The subsurface evolution provides additional evidence of how this transition developed across the equatorial Pacific (Figure 12). During September–November 2025, positive temperature anomalies were concentrated primarily in the western and central equatorial Pacific at approximately 100–200 m depth, while negative anomalies occupied the upper thermocline farther east. This produced a pronounced zonal contrast across the basin.

The subsurface structure changed substantially during early 2026. Positive anomalies progressively extended eastward while the negative anomalies of the central and eastern Pacific weakened. By March–April, warm anomalies had become increasingly prominent across the central Pacific and were extending toward the eastern basin. This transition accelerated during May–June, when a broad band of positive temperature anomalies extended eastward and upward along the equatorial thermocline.

By July–August 2026, strong positive temperature anomalies occupied much of the upper central and eastern equatorial Pacific and had become substantially shallower toward South America. The August section shows particularly strong warming across a broad portion of the eastern equatorial upper ocean. Together with the rapid increase in the ENSO indices, this evolution indicates a major reorganisation of the tropical Pacific upper ocean during the first half of 2026 and the establishment of El Niño conditions by the end of the ESR reporting period.

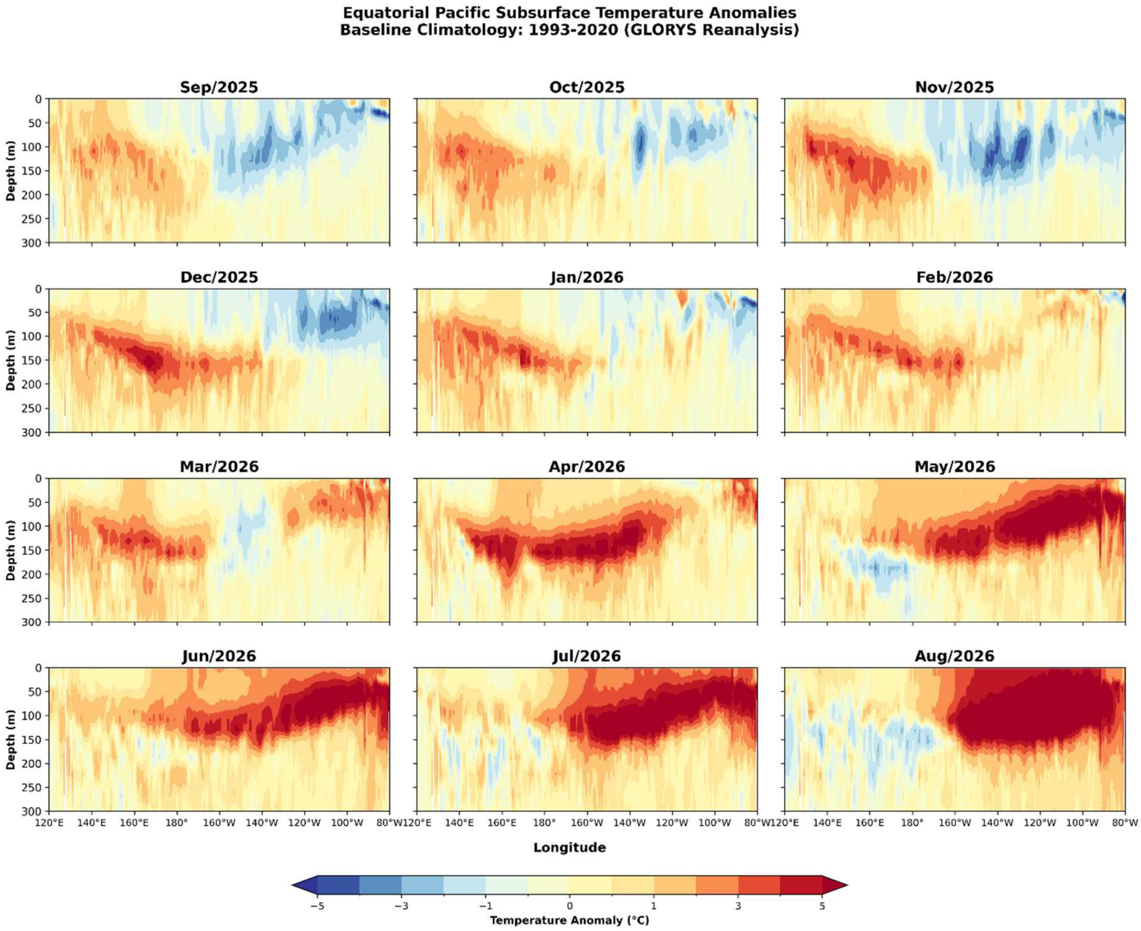

Figure 12. Monthly longitude–depth sections of equatorial Pacific subsurface temperature anomalies from September 2025 to August 2026, relative to the 1993–2020 climatology. Positive (red) and negative (blue) anomalies are expressed in °C. The sequence shows the progressive eastward and upward expansion of warm subsurface waters during early 2026, culminating in strong positive temperature anomalies throughout the upper central and eastern equatorial Pacific by July–August 2026.

8.3. Regional expression across the Southeast Pacific

The regional environmental indicators examined in this ESR show that the developing tropical Pacific signal was expressed unevenly across the Southeast Pacific. Its clearest manifestations occurred in the Equatorial High Seas and Northern Humboldt regions, particularly in temperature and sea level.

By August 2026, SST anomalies reached approximately +3.83°C in the Equatorial High Seas and +3.17°C in Northern Humboldt. Positive anomalies were also present farther south but decreased progressively in magnitude, reaching approximately +1.77°C in Northern Chile, +0.81°C in Central-Southern Chile, and +0.75°C in the Oceanic Southeast Pacific. This pronounced meridional gradient indicates that the strongest surface warming remained concentrated in the northern part of the ESR domain.

Sea level exhibited an even clearer spatial gradient. By August 2026, detrended SLA reached approximately +21.11 cm in the Equatorial High Seas and +8.03 cm in Northern Humboldt, compared with +2.14 cm in Northern Chile. Central-Southern Chile remained close to climatological conditions, whereas the Oceanic Southeast Pacific showed slightly negative SLA. The monthly spatial fields similarly documented the progressive development of elevated sea level in the equatorial and northern sectors during the first half of 2026, with the signal becoming particularly pronounced from May onward.

Other ecosystem-related indicators showed less spatially coherent responses. Coastal upwelling anomalies at the end of the reporting period were negative in all three coastal regions analysed, with the largest negative departure occurring in Northern Humboldt, indicating weaker-than-average wind-driven offshore Ekman transport. Chlorophyll-a did not exhibit an equivalent basin-wide response: August 2026 concentrations were slightly below climatology in Northern Humboldt and Northern Chile, slightly above climatology in the Equatorial High Seas and Central-Southern Chile, and close to climatological conditions in the Oceanic Southeast Pacific.

Taken together, the indicators show that by August 2026 the clearest regional expression of the developing El Niño occurred in upper-ocean temperature and sea level, and was concentrated in the equatorial and northern sectors. The weaker and less spatially coherent responses in upwelling and chlorophyll-a emphasise that biological and coastal responses cannot be assumed to track ENSO indices directly and should continue to be evaluated at the regional scale.

8.4. ENSO outlook

The NOAA CPC outlook issued in August 2026 indicates a very high probability that El Niño will persist beyond the end of the present ESR reporting period (Figure 13). El Niño probabilities reach essentially 100% from JAS through JFM, remaining approximately 97% in FMA and 82% in MAM. Neutral conditions become increasingly probable only toward the latter part of the forecast horizon, while the probability of La Niña remains negligible.

The event-strength probabilities indicate that the principal uncertainty concerns the eventual magnitude of El Niño rather than its occurrence. The probability distribution shifts strongly toward the strong and very strong El Niño categories during late 2026, particularly around OND and NDJ. Weaker categories become progressively more important thereafter as the event is forecast to decline during early 2027.

The RONI forecast provides a consistent picture. The ensemble mean increases from approximately +1.8°C in JAS to +2.6–2.7°C around OND, remains strongly positive through NDJ, and then decreases progressively during early 2027. Forecast uncertainty increases with lead time, however, and the probability intervals encompass a substantial range of possible event magnitudes.

The ESR therefore ends at a particularly important transition point. By August 2026, multiple observational indicators already show a rapidly developing warm event, including the sharp rise in RONI and MEI.v2, eastward and upward expansion of subsurface warming, strong SST anomalies, and elevated sea level in the equatorial and northern Southeast Pacific. At the same time, the CPC outlook indicates that the event is expected to intensify further after the August 2026 endpoint of this report, with strong-to-very-strong conditions favoured during late 2026.

Consequently, the environmental and ecosystem responses documented in this ESR should be regarded as representing the developmental phase of the 2026 El Niño rather than its complete evolution. Continued monitoring during the next ESR period will be important for assessing the subsequent regional expression of the event, particularly its effects on upper-ocean structure, coastal upwelling, oxygen conditions and primary productivity.

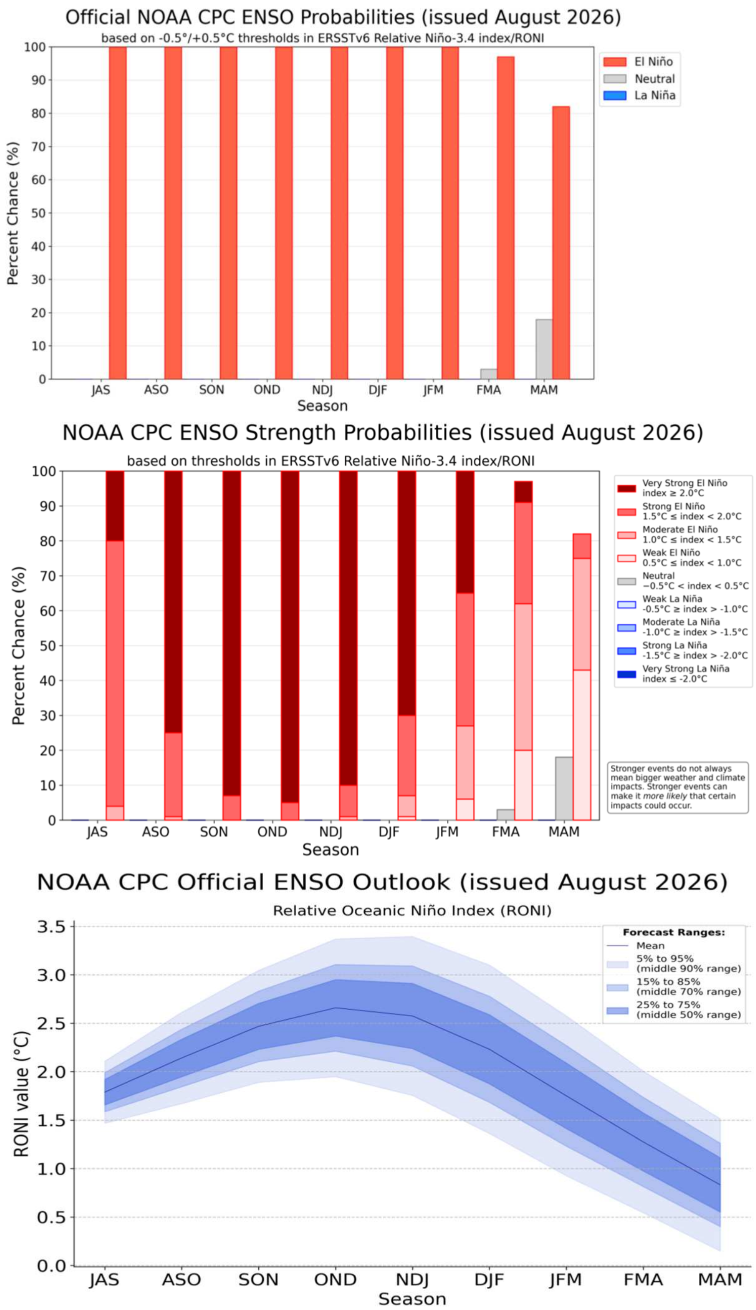

Figure 13. NOAA Climate Prediction Center (CPC) ENSO outlook issued in August 2026. Top: probabilities of El Niño, neutral, and La Niña conditions for successive three-month seasons, based on the ERSSTv6 Relative Niño-3.4 Index (RONI). Middle: probabilities of different ENSO strength categories, indicating an increasing likelihood of strong to very strong El Niño conditions during late 2026. Bottom: forecast evolution of RONI, showing the ensemble mean and the 50%, 70%, and 90% probability ranges. The outlook indicates a very high probability of El Niño persistence and further intensification during late 2026, followed by a projected weakening during early 2027.

References.

Hobday, A.J., Alexander, L.V., Perkins, S.E., Smale, D.A., Straub, S.C., Oliver, E.C.J., Benthuysen, J.A., Burrows, M.T., Donat, M.G., Feng, M., Holbrook, N.J., Moore, P.J., Scannell, H.A., Sen Gupta, A., & Wernberg, T. (2016). A hierarchical approach to defining marine heatwaves. *Progress in Oceanography*, 141, 227–238.

Hobday, A.J., Oliver, E.C.J., Sen Gupta, A., Benthuysen, J.A., Burrows, M.T., Donat, M.G., Holbrook, N.J., Moore, P.J., Thomsen, M.S., Wernberg, T., & Smale, D.A. (2018). Categorizing and naming marine heatwaves. *Oceanography*, 31(2), 162–173.